ELSEVIER

Computer Physics Communications 86 (1995) 25–39

Computer Physics Communications

Finite element simulation of a turbulent MHD system: comparison to a pseudo-spectral simulation

Rosalinda de Fainchtein [a], Steven T. Zalesak [b], Rainald Löhner [c], Daniel S. Spicer [b]

[a] *Universities Space Research Association, NASA Goddard SFC, Greenbelt, MD 20771, USA*

[b] *Center for Computational Sciences, NASA Goddard SFC, Greenbelt, MD 20771, USA*

[c] *Institute for Computational Sciences and Informatics, The George Mason University, Farifax, VA 22030, USA*

Received 15 April 1994; revised 12 October 1994

Abstract

A finite element MHD algorithm is used to simulate a two-dimensional, viscous and resistive turbulent model, namely the Orszag–Tang vortex. The results are compared to a pseudo-spectral simulation of the same system reported by Dahlburg and Picone (Phys. Fluids B 1 (1989) 2153). The agreement of results from both methods supports the contention that the finite element method can appropriately simulate systems exhibiting turbulence, thus enabling the use of realistic geometries and boundary conditions, as well as adaptive refinement on simulations of turbulent systems. A short discussion on the behavior of $\nabla \cdot \boldsymbol{B}$ is presented. An inverse correlation between spatial resolution and the magnitude of $\nabla \cdot \boldsymbol{B}$ was found. The relevance of our findings to Adaptive Mesh Refinement is briefly discussed.

1. Introduction

Fourier-based spectral and pseudo-spectral (PS) algorithms have traditionally been the method of choice to simulate turbulent systems [1,2]. This is because of the high accuracy of the method over the range of Fourier spatial wavenumbers (k-modes). However, the method imposes severe limitations on the kind of systems to be modeled. The method requires the use of a uniform static grid, as well as periodic, or at best semi-periodic boundary conditions. Spectral methods based on other than Fourier modes allow more flexibility on the choice of boundary conditions, but retain stiff requirements on the grid layout. Spectral element methods [2] represent a promising attempt to harness the flexibility benefits of the finite element (FE) method discussed here, while keeping the high accuracy of the spectral methods. It is a complex method that is relatively complicated to code, and for which adaptive refinement techniques are not fully developed.

The FE method offers the flexibility of unstructured meshes, as well as realistic geometries and boundary conditions [6,7]. Moreover, with unstructured meshes, higher spatial resolution can be allocated where it is needed, leaving a coarser grid on other regions of the domain. This allocation can either be done statically, or dynamically, by using adaptive mesh refinement (AMR) [8–10]. Finite element simulations have proven to be efficient and reliable in simulating various types of hydrodynamic systems, including supersonic shocks, and fluid flow around objects [11–14], as well as viscous and subsonic flows [15]. Lately, FE simulations of realistic magnetohydrodynamic (MHD) systems, such as the magnetosphere, have been reported [16].

SSDI 0110-4655(94)00143-X

In order to validate the use of the FE method for simulations of MHD turbulent systems, it is useful to test it against a PS simulation of a well researched turbulent MHD system. The Orszag–Tang vortex [17] is a good model for MHD turbulence that has been extensively studied [18–25]. It offers the advantage of quickly evolving turbulence, starting from simple analytical initial conditions. Because no noise is applied to the initial conditions, numerical solutions of the Orszag–Tang vortex system are reproducible, making it an excellent test problem with which to evaluate a FE turbulent simulation.

In the rest of this paper we present the results of the comparison of a FE simulation to the PS simulation of a compressible version of the Orszag–Tang vortex, reported by Dahlburg and Picone [22]. The next section formulates the MHD problem. We then explain the initial conditions. A brief description of the FE algorithm is then given, followed by a comparison of results and analysis, and finally some conclusions.

2. Formulation

The magnetohydrodynamic (MHD) equations of motion for a two-dimensional viscous and resistive magnetofluid are

$$\frac{\partial \rho}{\partial t} = -\nabla \cdot (\rho \boldsymbol{v}), \tag{1}$$

$$\frac{\partial \rho \boldsymbol{v}}{\partial t} = -\nabla \cdot \left[\rho \boldsymbol{v}\boldsymbol{v} + \left(p + \frac{B^2}{8\pi}\right)\boldsymbol{I} - \frac{1}{4\pi}\boldsymbol{B}\boldsymbol{B}\right] + \nabla \cdot \tau, \tag{2}$$

$$\frac{\partial \boldsymbol{B}}{\partial t} = \nabla \times [(\boldsymbol{v} \times \boldsymbol{B}) - \eta \nabla \times \boldsymbol{B}], \tag{3}$$

$$\frac{\partial U}{\partial t} = -\nabla \cdot \left[\left(U - \frac{B^2}{8\pi} + p\right)\boldsymbol{v} - \frac{1}{4\pi}(\boldsymbol{v} \times \boldsymbol{B}) \times \boldsymbol{B}\right] + \nabla \cdot [(\boldsymbol{v} \cdot \tau + (\gamma\mu/\mathrm{Pr})\nabla e) - (\eta/8\pi)(\nabla(\boldsymbol{B} \cdot \boldsymbol{B}) - 2(\boldsymbol{B} \cdot \nabla)\boldsymbol{B})]. \tag{4}$$

Supplemented by the equation of state

$$p = (\gamma - 1)\rho e. \tag{5}$$

The dynamical variables $\rho, \boldsymbol{v}, \boldsymbol{B}, U$ are the mass density, velocity, magnetic induction field, and total energy, respectively. The rest of the notation is as follows: p is the mechanical pressure, e is the internal energy per unit mass, $\boldsymbol{I}$ is the unit dyad, τ is the viscous stress tensor

$$\tau = \mu[(\partial_j v_i + \partial_i v_j) - \tfrac{2}{3}\nabla \cdot \boldsymbol{v}\delta_{ij}]\boldsymbol{e}_i\boldsymbol{e}_j, \tag{6}$$

μ is the viscosity, $\boldsymbol{e}_i$ and $\boldsymbol{e}_j$ are standard unit vectors, $\gamma = 5/3$ is the ratio of specific heats, η is the magnetic diffusivity, Pr is the Prandtl number $\mathrm{Pr} = c_p\mu/k$, c_p is the specific heat at constant pressure, and k is the thermal conductivity. Dahlburg and Picone use reduced units in their simulation. The correspondence to cgs units is as follows, with the starred variables corresponding to dimensionless units. Length, time and mass are equivalent: $L = L^*$, $t = t^*$, $\rho = \rho^*$, $\boldsymbol{v} = \boldsymbol{v}^*$. The rest of the variable correspondence is: $\boldsymbol{B} = \sqrt{4\pi}\boldsymbol{B}^*$ $p = p^*/2$, $U = U^*/2$, $kT \equiv (\gamma\mu/\mathrm{Pr})e = [\mu/(\mu - 1)](\mu/\mathrm{Pr})T^*/2$, $\boldsymbol{J} = \sqrt{4\pi}\boldsymbol{J}^*$. The dimensionless Lundquist resistive and viscous numbers, S_r and S_v correspond to inverse magnetic diffusivity and viscosity, respectively, on this particular problem.

The finite element code is capable of running on an arbitrary grid, and can handle realistic boundary conditions. However, for comparison purposes, we used the same regular 128×128 grid on a square domain of side length of 2π and periodic boundary conditions used by Dahlburg and Picone on their pseudo-spectral simulations. We report on comparison results $S_r = S_v = 100$ and $\mathrm{Pr} = 1$.

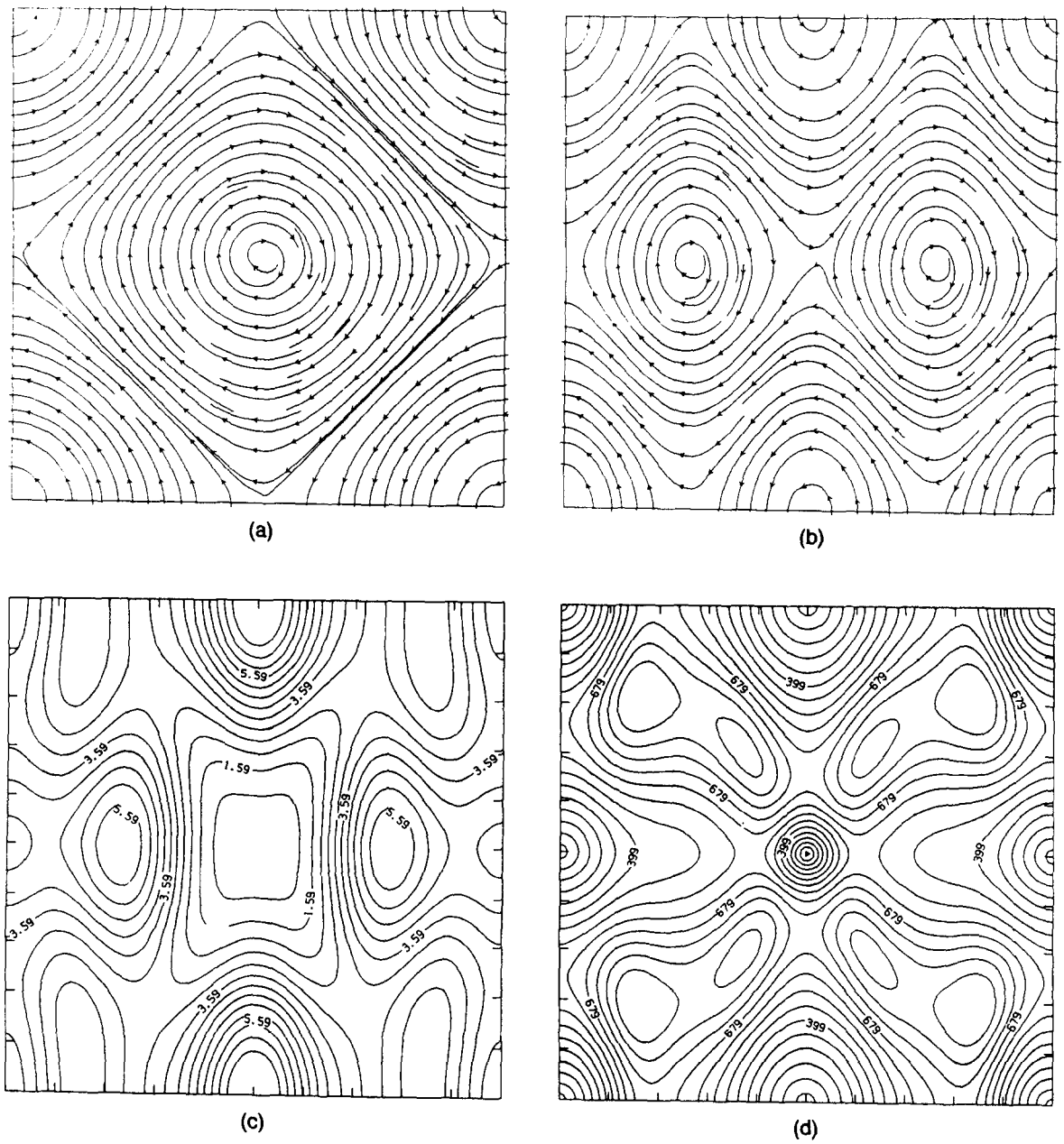

Fig. 1. Initial Conditions: (a) velocity field; (b) magnetic field; initial conditions specific to the $M = 0.6$ case: (c) thermal pressure field; (d) local Mach number. Minimum and maximum values are 0.73 and 7.9 for thermal pressure and 0.0 and 0.97 for local Mach number [22].

3. Initial conditions

The initial conditions corresponding to the Orszag–Tang vortex are as follows,

$$\rho(x, y, t = 0) = 1, \tag{7}$$

$$\boldsymbol{v}(x, y, t=0) = -\sin(y)\hat{\boldsymbol{x}} + \sin(x)\hat{\boldsymbol{y}}, \tag{8}$$

$$\boldsymbol{B}(x, y, t=0) = -\sqrt{4\pi}\sin(y)\hat{\boldsymbol{x}} + \sqrt{4\pi}\sin(2x)\hat{\boldsymbol{y}}, \tag{9}$$

After accounting for the difference in normalization the initial pressure field is identical on both simulations;

$$p(x, y, t=0) = \frac{1}{\gamma M^2} + \tfrac{1}{4}\cos 4x + \tfrac{1}{4}\cos 2y + \tfrac{4}{5}\cos 2x \cos y - \cos x \cos y, \tag{10}$$

The "characteristic" Mach number M is obtained using domain averages of the initial density and pressure,

$$M^2 = \frac{\langle \rho(t=0) \rangle}{\gamma \langle p(t=0) \rangle}. \tag{11}$$

Dahlburg and Picone chose to use this initial pressure field to be consistent with the corresponding incompressible system. This allowed them to compare the compressible and incompressible behavior of the system.

Results with initial Mach numbers $M = 0.2$ and $M = 0.6$ are reported. They correspond to $\langle \beta \rangle \equiv 8\pi \langle p \rangle / \langle B \rangle^2 = 30.0$ and 3.3, respectively.

4. The numerical method

The finite element algorithm is based on a two-dimensional, two-step Taylor–Galerkin Method. The Taylor–Galerkin method is explained in detail by Donea [26] and Löhner et al. [27]. The use of two steps is described by Löhner et al. [28]. A viscous gas dynamics version of this code, due to Löhner [15] has been extensively tested [15,29]

Since this resistive MHD algorithm follows the same formalism described in the above named references, we limit ourselves to give only a brief description of the method. We begin by schematically representing the MHD equations in flux form. This simplifies the notation and provides consistency with the literature. It is also representative of the "strategy" of the method. Thus, we rewrite Eqs. (1)–(4) as

$$\frac{\partial \boldsymbol{w}}{\partial t} = -\nabla \cdot \boldsymbol{F}^{\mathrm{a}} - \nabla \cdot \boldsymbol{F}^{\mathrm{rv}}, \tag{12}$$

where

$$\boldsymbol{w} = \begin{Bmatrix} \rho \\ \rho \boldsymbol{v} \\ \boldsymbol{B} \\ U \end{Bmatrix}, \tag{13}$$

$$\nabla \cdot \boldsymbol{F}^{\mathrm{a}} = \begin{Bmatrix} \nabla \cdot (\rho \boldsymbol{v}) \\ \nabla \cdot \left[\rho \boldsymbol{v}\boldsymbol{v} + \left(p + \dfrac{B^2}{8\pi} \right) \boldsymbol{I} - \dfrac{1}{4\pi} \boldsymbol{B}\boldsymbol{B} \right] \\ -\nabla \times (\boldsymbol{v} \times \boldsymbol{B}) \\ \nabla \cdot \left[\left(U - \dfrac{B^2}{8\pi} + p \right) \boldsymbol{v} - \dfrac{1}{4\pi} (\boldsymbol{v} \times \boldsymbol{B}) \times \boldsymbol{B} \right] \end{Bmatrix}, \tag{14}$$

and

$$\nabla\cdot\boldsymbol{F}^{\mathrm{rv}} = \left\{ \begin{array}{c} 0 \\ -\nabla\cdot\tau \\ -\eta\nabla\cdot(\nabla\boldsymbol{B}) \\ -\nabla\cdot\left[\boldsymbol{v}\cdot\tau + \dfrac{\gamma\mu}{\mathrm{Pr}}\nabla e + \dfrac{\eta}{8\pi}\nabla\cdot(-B^2\boldsymbol{I} + 2\boldsymbol{BB})\right] \end{array} \right\}. \tag{15}$$

Notice that the inviscid ideal MHD terms are grouped together unto $\nabla\cdot\boldsymbol{F}^{\mathrm{a}}$ and the resistive and viscous terms unto $\nabla\cdot\boldsymbol{F}^{\mathrm{rv}}$. It is also important to note that this code advances the magnetic induction field $\boldsymbol{B}$, and that the condition $\nabla\cdot\boldsymbol{B} = 0$ is not strictly guaranteed. (We chose not to implement any of the available numerical techniques to "fix" this problem [3–5], in order to monitor the behavior of $\nabla\cdot\boldsymbol{B}$.)

The solution is advanced from t^n to $t^{n+1} = t + \Delta t$ in two steps. In the first step:

$$\boldsymbol{w}^{n+1/2} = \boldsymbol{w}^n - \frac{\Delta t}{2}(\nabla\cdot\boldsymbol{F}^{\mathrm{a}}\,|_n). \tag{16}$$

In the second step

$$\boldsymbol{w}^{n+1} = \boldsymbol{w}^n - \Delta t(\nabla\cdot\boldsymbol{F}^{\mathrm{a}}\,|_{n+1/2}) - \Delta t(\nabla\cdot\boldsymbol{F}^{\mathrm{rv}}\,|_n). \tag{17}$$

By using a classical Galerkin weighted residual method on a triangular mesh, [6,7] a spatial discretization of equations (16)and (17) above is obtained. Stability of the method is maintained much in the manner of the two-step Richtmyer variant of the Lax-Wendroff method [30]. This is achieved by choosing a basis of piecewise constant functions to interpolate half-step variables (e.g. $\boldsymbol{w}^{n+1/2}$), and a basis of piecewise linear functions to interpolate full step variables (e.g. $\boldsymbol{w}^n$). In the resulting weak form of Eq. (16), a local spatial average of $\boldsymbol{w}^n$ takes the place of $\boldsymbol{w}^n$ (this is analogous to the half grid point spatial staggering of the two-step Richtmyer algorithm), thus providing the necesary numerical diffusion to maintain stability. Our choice of basis functions eliminates the need for matrix operations on the first step, and yields the following matrix equation to be solved on the second step,

$$\boldsymbol{M}_{\mathrm{c}}\Delta\boldsymbol{w} = \boldsymbol{f}. \tag{18}$$

Here $\boldsymbol{M}_{\mathrm{c}}$ is the consistent mass matrix [6,7], and $\boldsymbol{f}$ represents the summed element contributions to each node arising from the flux terms [28]. The mass matrix equation (Eq. (18)) is solved explicitly by an iterative method [26,27].

For comparison purposes, the simulations are made on a uniform triangular mesh with periodic boundary conditions. The element nodes are positioned to correspond exactly to the uniform 128 × 128 mesh used by Dahlburg and Picone. We use a variable time step determined dynamically by a Courant condition

$$\Delta t = \min\left\{ \frac{Nh}{(1 + 2N/hR)(\sqrt{C_{\mathrm{s}}^2 + V_{\mathrm{A}}^2} + |\boldsymbol{v}|)} \right\}, \tag{19}$$

where h is the nearest node distance, $N = 0.25$, C_{s} is the speed of sound, and V_{A} is the Alfvèn speed. The Courant condition is somewhat different from the one used in the PS simulation. However, the resulting time steps on both simulations are comparable. The FE simulation was performed on the NCCS Cray-YMP Supercomputer. The approximate CPU usage per node per time step was 36 μs.

Dahlburg and Picone chose to advance the vector potential $\boldsymbol{A}$ in their PS simulation, thus insuring that $\nabla\cdot\boldsymbol{B} = 0$ throughout the domain. Since we are comparing to a simulation where $\nabla\cdot\boldsymbol{B} = 0$ is strictly enforced, any errors caused by a nonzero divergence of $\boldsymbol{B}$ in the FE simulation will be bound by the difference between the results of the two simulations. In this context, it becomes useful to contrast the behavior of $\nabla\cdot\boldsymbol{B}$ in

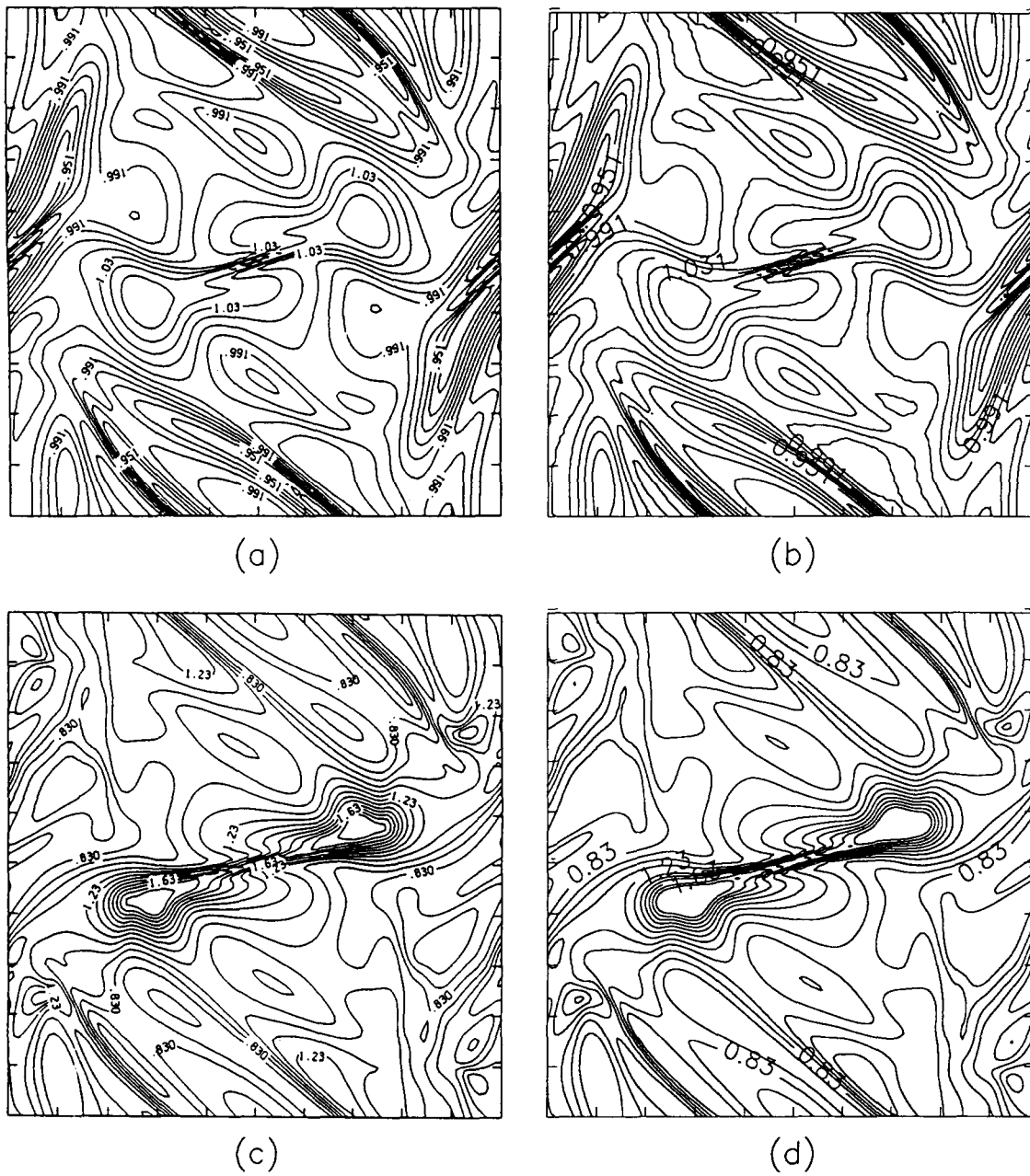

Fig. 2. Comparison of PS and FE contour plots of mass density, $S = 100$: (a) PS, $M = 0.2$, $t = 2$; (b) FE, $M = 0.2$, $t = 2$; (c) PS, $M = 0.6$, $t = 2$; (d) FE, $M = 0.6$, $t = 2$; (e) PS, $M = 0.6$, $t = 8$; (f) FE, $M = 0.6$, $t = 8$. (PS plots reproduced from Dahlburg and Picone [22].)

the FE simulation with the level of agreement between the two simulations. We report on the behavior of $\epsilon \equiv |\nabla \cdot \boldsymbol{B}|/\text{median}(|\boldsymbol{B}|)$ [1].

[1] Schmidt–Voigt [31,32] suggests using the parameter $B_{\text{rel}} \equiv h|\nabla \cdot \boldsymbol{B}|/|\boldsymbol{B}|$ as a diagnostic parameter for the error. However, since the Orszag–Tang Vortex solutions include points where $|\boldsymbol{B}| \sim 0$, B_{rel} is not an appropriate parameter for this problem.

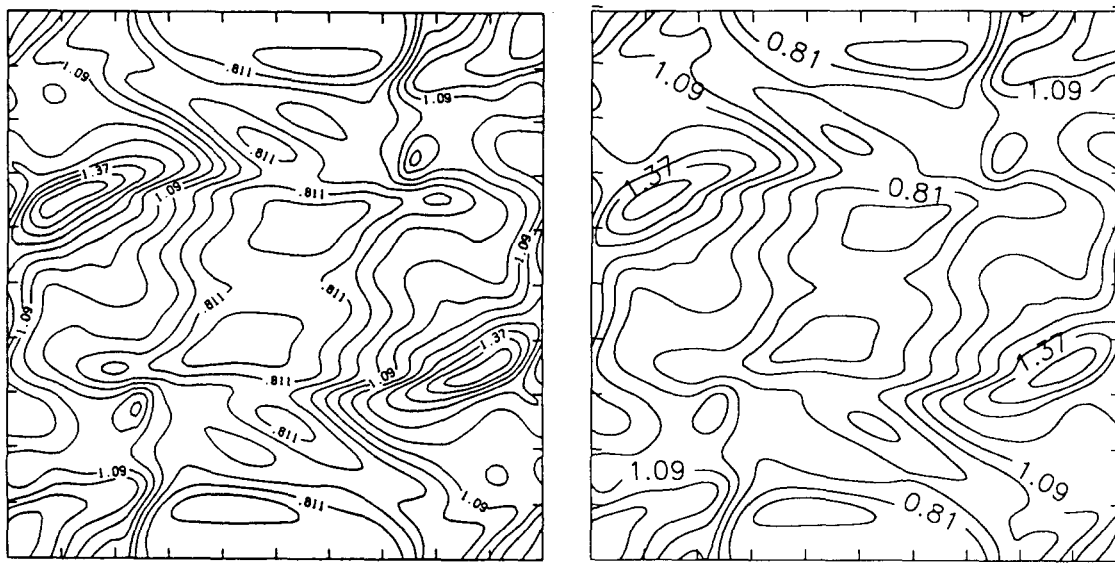

Fig. 2. Continued.

5. Results

In an attempt to make a thorough evaluation of the accuracy of our FE-MHD method against a pseudo-spectral method we compare contour plots, time evolution of global quantity plots, as well as k-spectra from both simulations. (In order to be consistent with the reported PS results, the plots are reported in reduced units (c.f. Formulation Section above).)

On Figs. 2 through 5 we show side by side FE versus PS contour plots of density, local rate of dilatation, vorticity, and current density at $t = 2$. The contour levels on the FE plots were chosen to match the values on the corresponding PS contour plots. The agreement of the results is immediately apparent. Even at $t = 8$, where both simulations have had more time to evolve, the density contours from both simulations, shown on Figs. 2e and 2f, show that the two methods demonstrate remarkable agreement.

The global quantities are averages of various physical variables over the whole domain at a fixed time. They are computed at regular time intervals. Fig. 6 shows comparisons of the time evolution of the various global quantities. The diamonds correspond to PS results. The continuous lines are computed using data at ~ 200 different times from the FE simulation. Fig. 6a is the cross helicity: $H_c \equiv \langle \boldsymbol{v} \cdot \boldsymbol{B} \rangle$, Fig. 6b is the averaged kinetic plus magnetic energy, Fig. 6c is the correlation coefficient: $\xi \equiv 2\langle \boldsymbol{v} \cdot \boldsymbol{B} \rangle / [\langle v^2 \rangle + \langle B^2 \rangle]$, Fig. 6d is the alignment factor $\alpha \equiv \langle \boldsymbol{v} \cdot \boldsymbol{B} \rangle / \sqrt{\langle v^2 \rangle \langle B^2 \rangle}$, Fig. 6e is the kinetic energy, Fig. 6f is the magnetic energy, Fig. 6g is the kinetic enstrophy: $\langle \omega^2 \rangle; \omega = \nabla \times \boldsymbol{v}$, and Fig. 6h is the magnetic enstrophy: $\langle j^2 \rangle$, where $\boldsymbol{j}$ is the current density. The L1-norm of the difference between PS and FE results for each global quantity was computed as $L1(f) = \sum |f^{FE} - f^{PS}| / \sum |f^{PS}|$, with the sums being over all the times reported on the PS simulation (at the diamonds). Note that except for the kinetic and magnetic enstrophy, the agreement between FE and PS time evolution plots is nearly perfect. The small discrepancies on the kinetic and magnetic enstrophy (Figs. 6g and 6h) is probably due to the larger weight with which the higher k-modes contribute to these quantities [33].

The k-spectra from FE and PS simulations are presented side by side on Figs. 7 through 9. A line derived by tracing through the center of the corresponding PS spectrum is overlayed on each FE spectrum in order to aid the comparison. Fig. 7 shows the mass density spectra, Fig. 8 the magnetic energy spectra, and Fig. 9 the solenoidal and non-solenoidal energy spectra. The main feature on these plots is that the FE spectra follow very

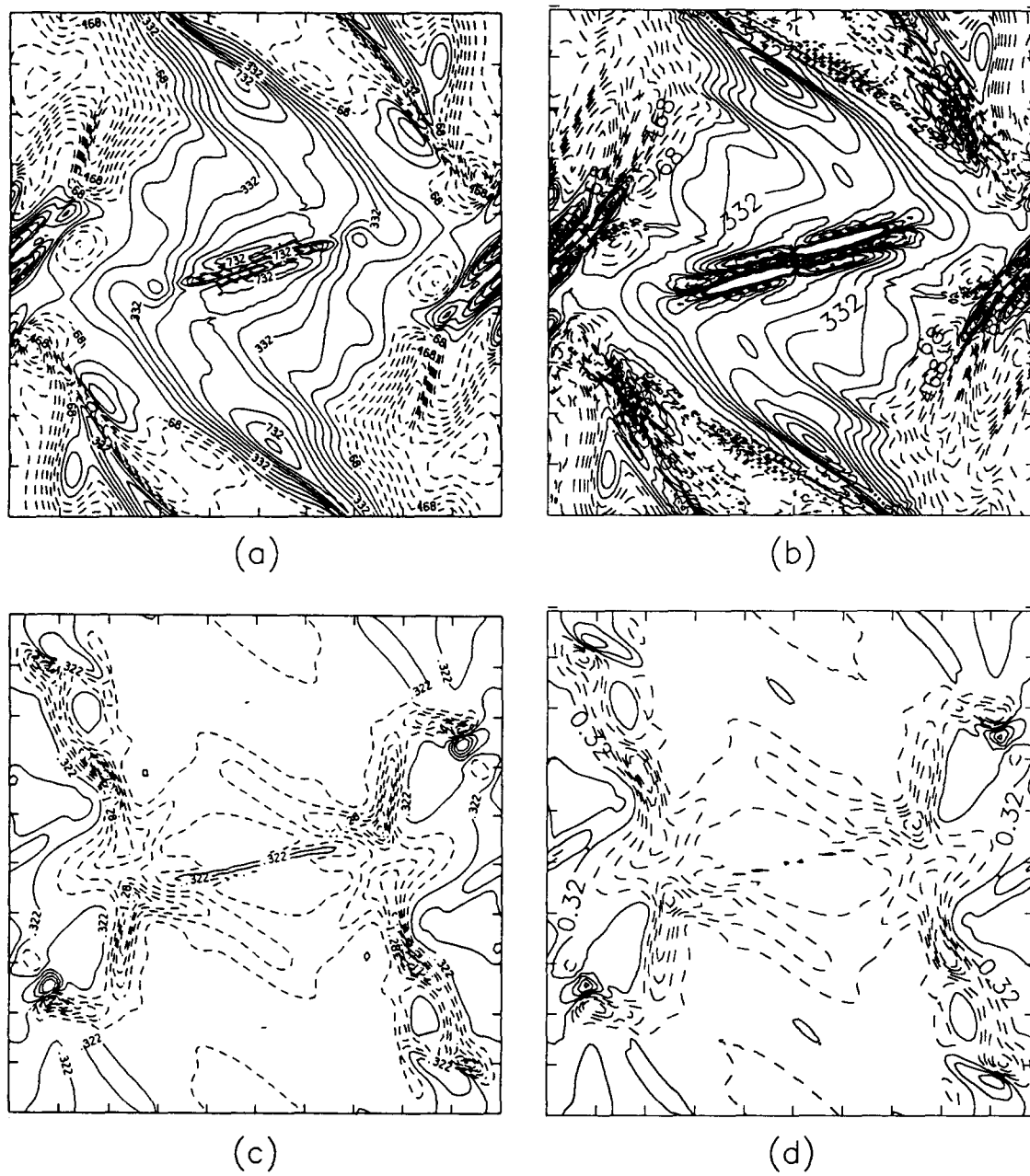

Fig. 3. Comparison of PS and FE contour plots of the local rate of dilatation ($S = 100$): (a) PS, $M = 0.2$, $t = 2$; (b) FE, $M = 0.2$, $t = 2$; (c) PS, $M = 0.6$, $t = 2$; (d) FE, $M = 0.6$, $t = 2$. Minimum and maximum contour values are (a) −0.107 and 0.104, (b) −0.132 and 0.250, (c) −4.01 and 2.58, and (d) −2.64 and 2.04. (PS plots reproduced from Dahlburg and Picone [22].)

closely the PS spectra. Significant discrepancies appear only at the large-k end of the spectra ($k^2 > 1000$). The sharp flattening at the "tails" of some of the FE spectra, particularly on the magnetic energy spectrum at $t = 8$ on Fig. 8f, suggest the presence of aliasing at $k^2 > 1000$. The PS spectra do not exhibit this flattening, presumably because aliasing is avoided on the PS simulation by isotropic truncation in Fourier space at each

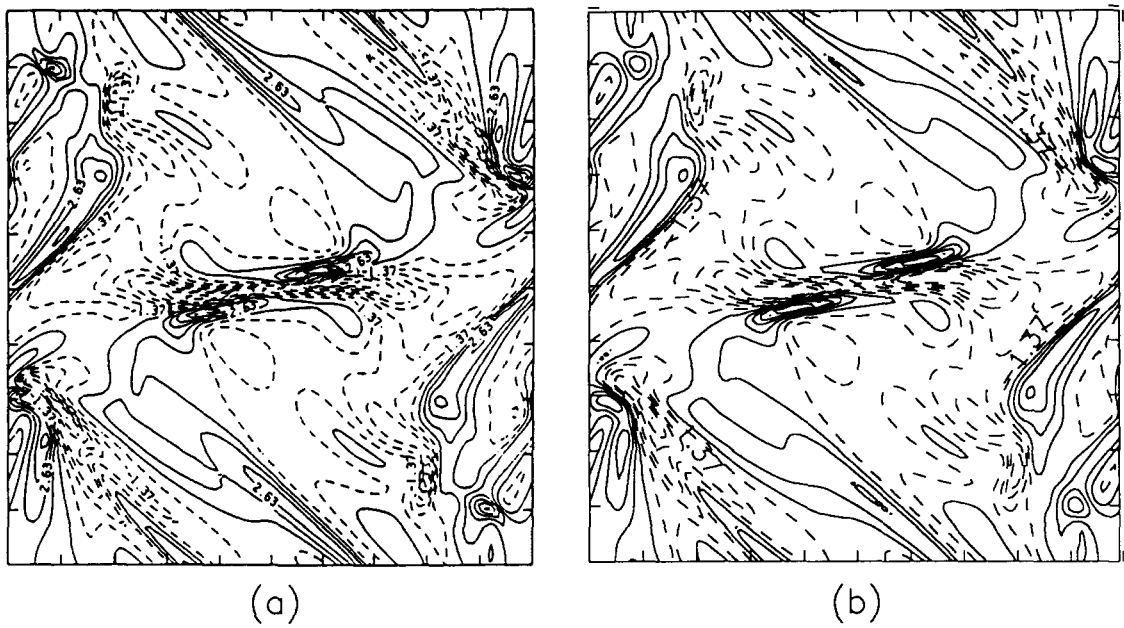

Fig. 4. Comparison of PS and FE contour plots of vorticity ($S = 100$): (a) PS, $M = 0.6$, $t = 2$; (b) FE, $M = 0.6$, $t = 2$; . Minimum and maximum contour values are (a) -8.10 and 6.45, and (b) -7.14 and 5.74. (PS plots reproduced from Dahlburg and Picone [22].)

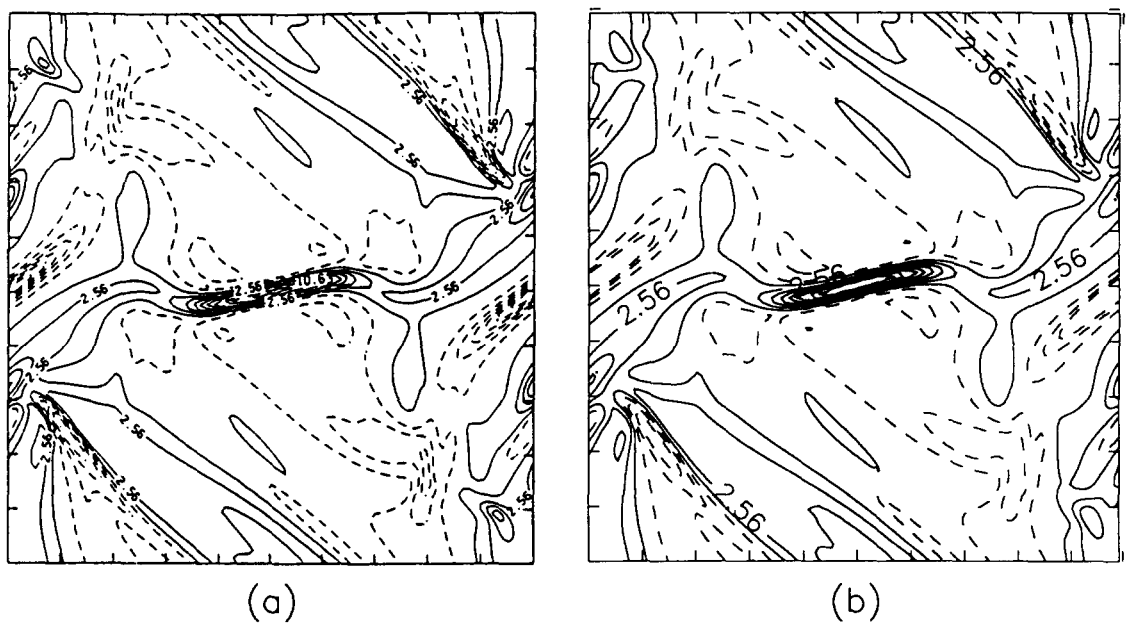

Fig. 5. Comparison of PS and FE contour plots of current density ($S = 100$): (a) PS, $M = 0.6$, $t = 2$; (b) FE, $M = 0.6$, $t = 2$; . Minimum and maximum contour values are (a) -13.1 and 20.4, and (b) -12.9 and 17.2. (PS plots reproduced from Dahlburg and Picone [22].)

time level. The finite element spectra are somewhat noisier. The noise is probably highlighted by plotting against k^2, instead of k.

Fig. 10 shows plots of $\nabla \cdot \boldsymbol{B}$ divided by the norm of the magnetic field magnitude ($\epsilon = \nabla \cdot \boldsymbol{B}/|\boldsymbol{B}|_{\text{med}}$) for the FE simulation for $M = 0.2$, at $t = 2$, and $M = 0.6$, at $t = 2$ and $t = 8$, respectively. In order to facilitate the

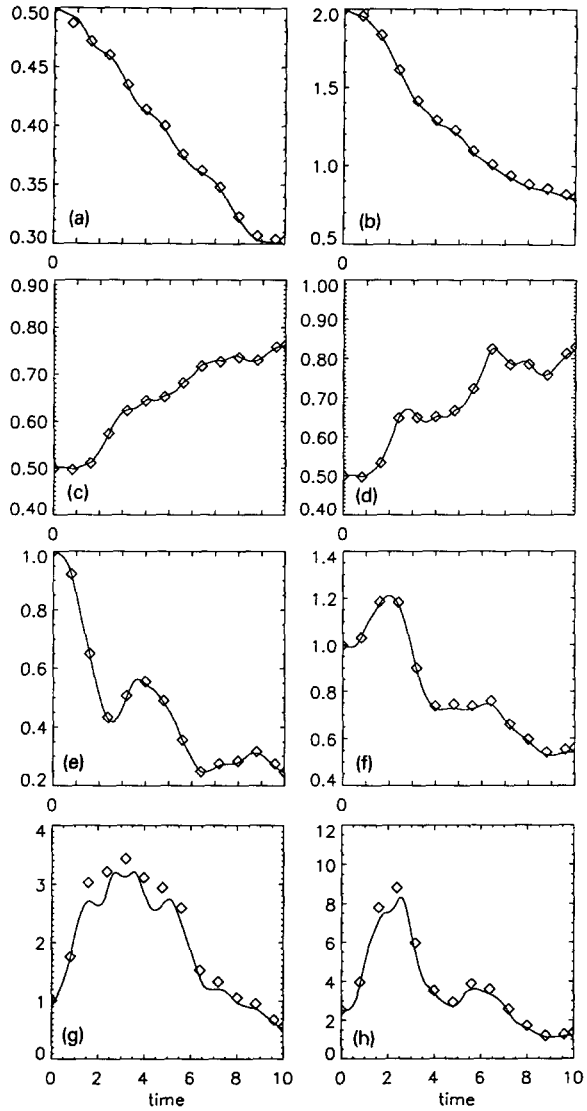

Fig. 6. Time evolution of global quantities. $M = 0.6$, $S = 100$ (diamonds correspond to PS results from Dahlburg and Picone [22]; lines correspond to FE results computed at 100 time intervals): (a) cross helicity, (b) kinetic plus magnetic energy, (c) correlation coefficient, (d) alignment factor, (e) kinetic energy, (f) magnetic energy, (g) kinetic enstrophy, and (h) magnetic enstrophy. L1-norms, as defined in the text are: (a)6.5×10^{-3}, (b)1.3×10^{-2}, (c)1.8×10^{-3}, (d)2.5×10^{-3}, (e)1.1×10^{-2}, (f)1.4×10^{-2}, (g)8.7×10^{-2}, and (h)7.4×10^{-2}, respectively.

analysis, only one contour level is plotted. The choice of the $\epsilon = 0.05$ contour level is arbitrary. On all three cases, $\epsilon < 0.05$ over most of the domain. For $t = 2$, the regions where ϵ is largest coincide with the location of the current sheets (c.f. Fig 5 versus Fig. 10b). Nevertheless, a review of the contour comparison of PS and FE simulations results (cf. Figs. 2–5) show good agreement at the locations of the current sheets (as well as the rest of the domain).

The current sheets are particularly interesting on studies of reconnection, and are likely to require the highest spatial resolution on the domain. If AMR was implemented, it would be desirable to target for refinement the regions of the domain where current sheets are found. The question of how ϵ behaves as the spatial

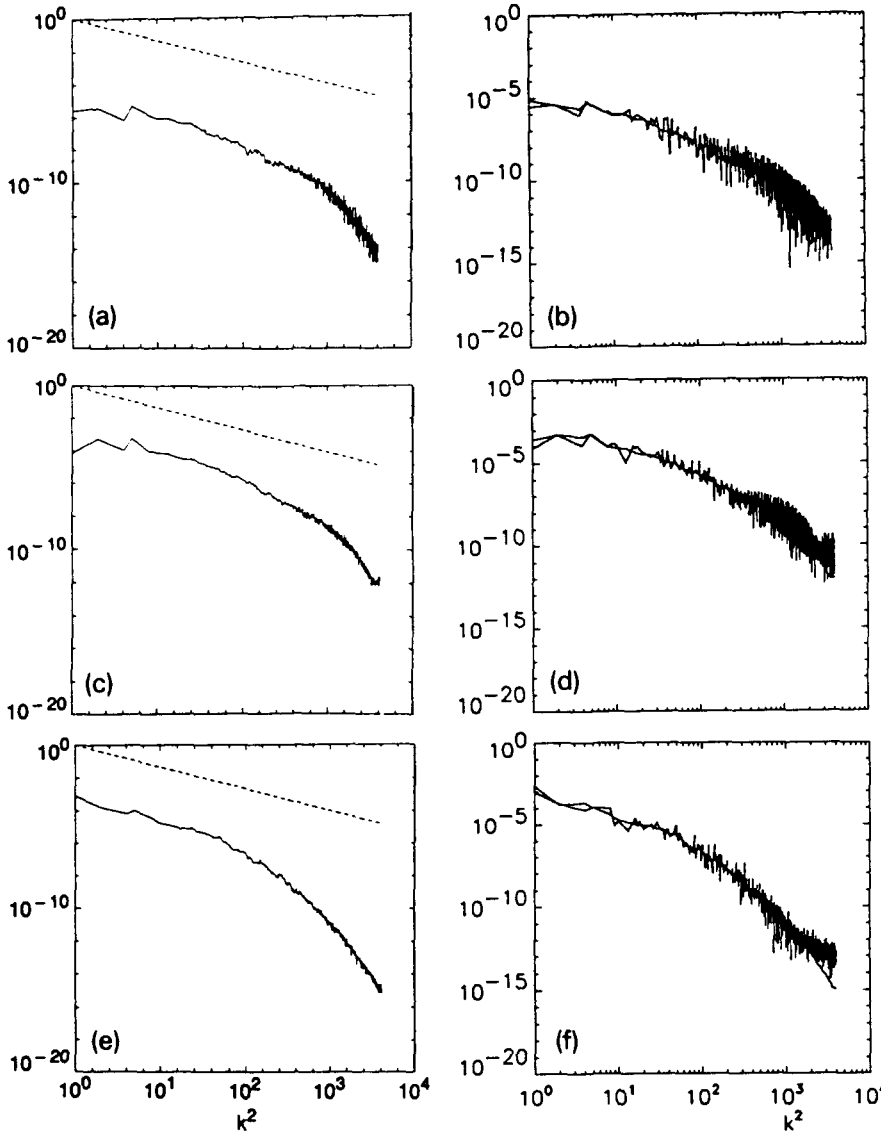

Fig. 7. Comparison of PS and FE k-spectra of mass density ($S = 100$): (a) PS, $M = 0.2$, $t = 2$; (b) FE, $M = 0.2$, $t = 2$; (c) PS, $M = 0.6$, $t = 2$; (d) FE, $M = 0.6$, $t = 2$; (e) PS, $M = 0.6$, $t = 8$; (f) FE, $M = 0.6$, $t = 8$. (PS plots reproduced from Dahlburg and Picone [22]. See text.)

resolution changes becomes important. To address this question we computed ϵ for simulations of identical initial conditions and parameters, but different resolution. We found that ϵ decreased with increasing spatial resolution. Figs. 11a and 11b are both plots of ϵ for FE simulations with $M = .6$, $S = 100$ at $t = 2$. Fig. 11a corresponds to a simulation on a 64×64 grid, whereas Fig. 11b corresponds to a simulation on a 128×128 grid (the same size grid used on the rest of the simulations reported). Although it is not immediately apparent form the figures, the portion of the domain where $\epsilon > 0.05$ is four times bigger on Fig. 11a (low resolution) than on Fig. 11b (high resolution). Moreover, the maximum value of ϵ also decreased by a factor of two as the resolution was doubled.

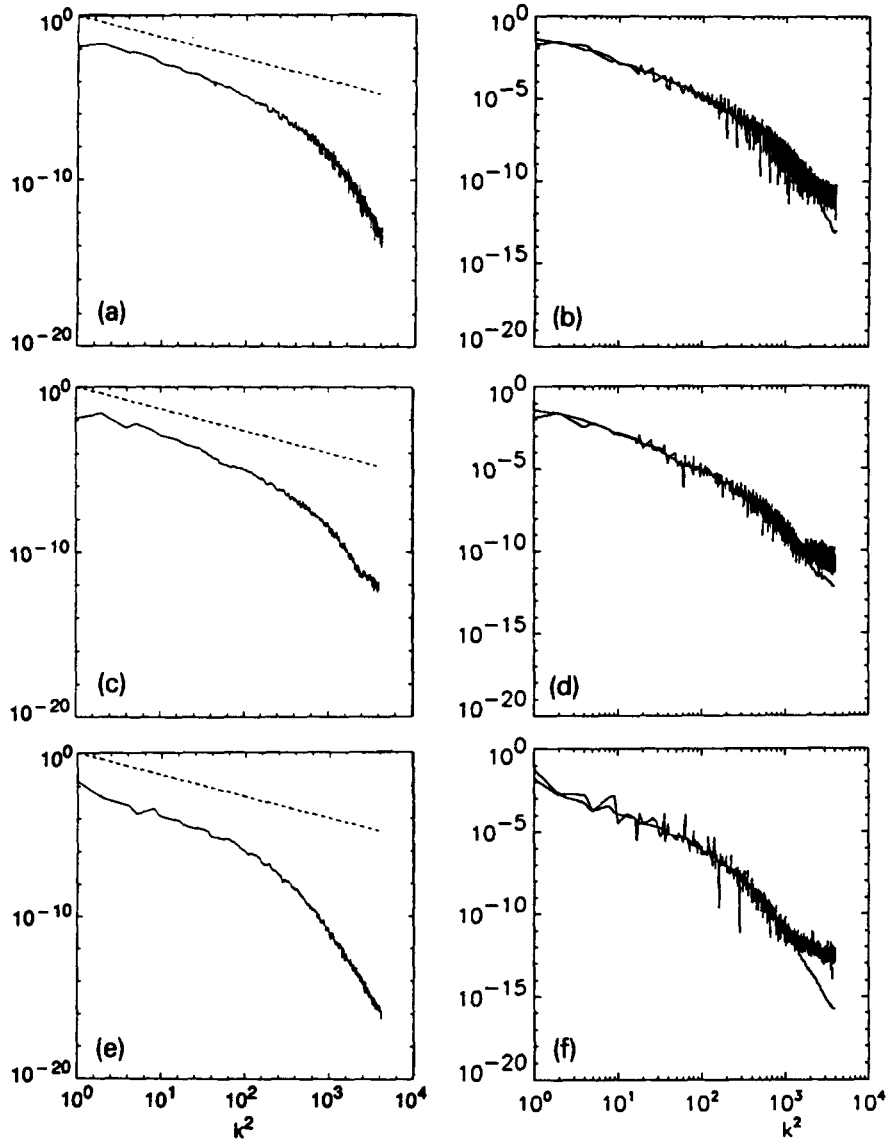

Fig. 8. Comparison of PS and FE k-spectra of magnetic energy ($S = 100$): (a) PS, $M = 0.2$, $t = 2$; (b) FE, $M = 0.2$, $t = 2$; (c) PS, $M = 0.6$, $t = 2$; (d) FE, $M = 0.6$, $t = 2$; (e) PS, $M = 0.6$, $t = 8$; (f) FE, $M = 0.6$, $t = 8$. (PS plots reproduced from Dahlburg and Picone [22]. See text.)

6. Conclusions

By using an MHD-FE simulation, we have reproduced very closely the results reported by Dahlburg and Picone of a PS simulation of a turbulent MHD system, thus showing that a FE-MHD method can be effective on simulating turbulent systems. This is an important finding, given that the flexibility of the FE method could allow simulations of turbulent systems with realistic geometries and boundary conditions. Moreover, with unstructured grids and adaptive refinement, simulations of problems where very small scale phenomena occur on small regions of the domain (e.g. reconnection) can be tackled by allocating the fine grid resolution only when and where it is needed.

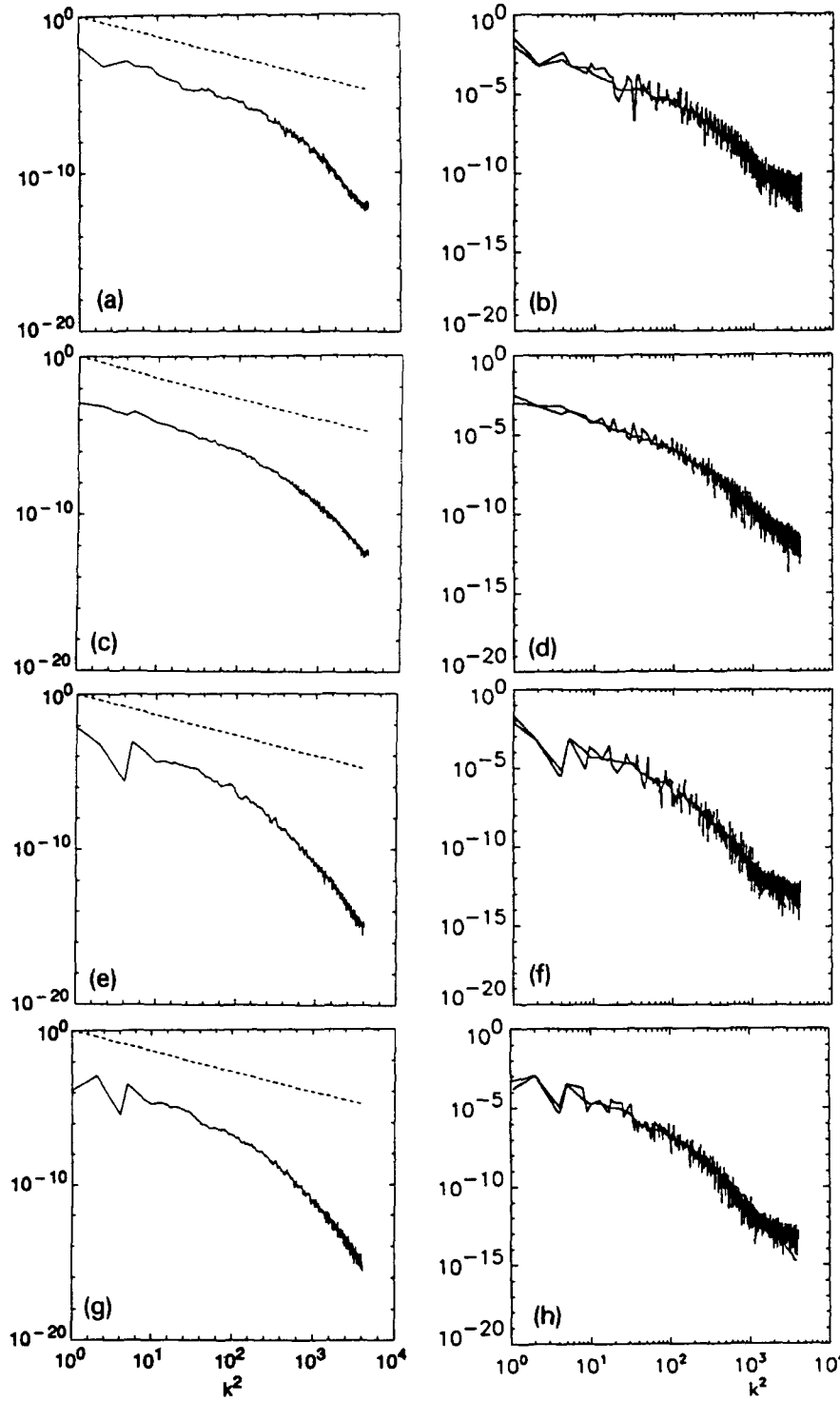

Fig. 9. Comparison of PS and FE k-spectra of solenoidal and non-solenoidal kinetic energy ($M = 0.6$, $S = 100$): (a) PS, solenoidal, $t = 2$; (b) FE, solenoidal, $t = 2$; (c) PS, non-solenoidal, $t = 2$; (d) FE, non-solenoidal, $t = 2$; (e) PS, solenoidal, $t = 8$; (f) FE, solenoidal, $t = 8$; (g) PS, non-solenoidal, $t = 8$; and (h) FE, non-solenoidal, $t = 8$. (PS plots reproduced from Dahlburg and Picone [22]. See text.)

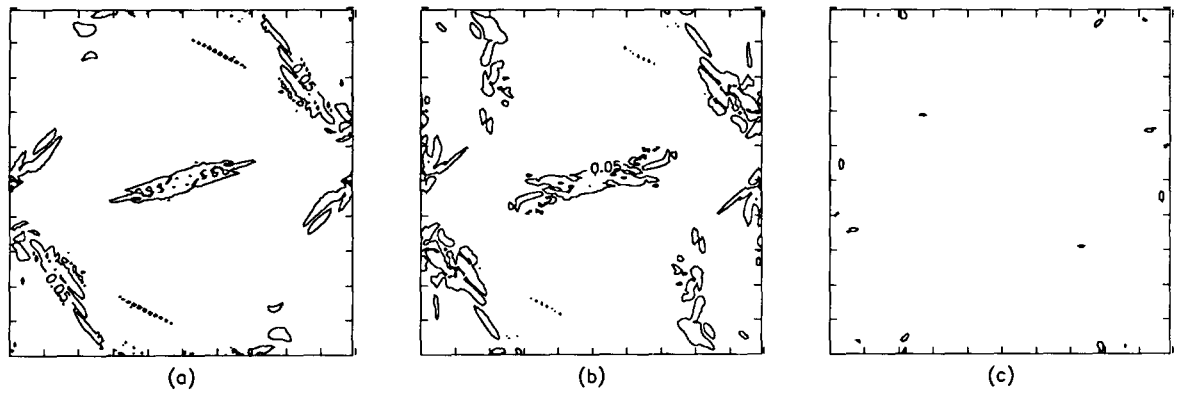

Fig. 10. Contour plots of ϵ from the FE simulations ($S = 100$): (a) $M = 0.2$, $t = 2$, (b) $M = 0.6$, $t = 2$, and (c) $M = 0.6$, $t = 8$. Minimum, maximum, and median contour values are (a) 0.0, 0.78, and 0.0086, (b) 0.0, 0.71, and 0.010, and (c) 0.0, 0.089, and 0.0077.

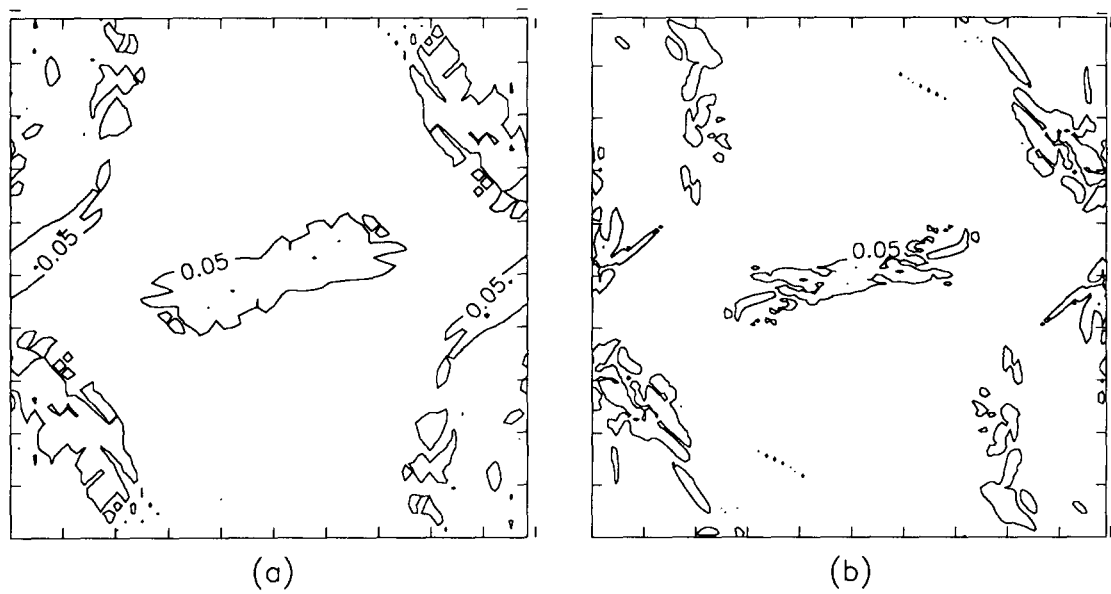

Fig. 11. Comparison of contour plots of ϵ from FE simulations performed at different spatial resolutions ($M = 0.6$, $t = 2$, $S = 100$): (a) 64×64 grid , (b) 128×128 grid. Minimum, maximum, and median contour values are (a) 0.0, 1.53, and 0.014, (b) 0.0, 0.71, and 0.010. Percentage of the domain where $\epsilon > 0.05$: (a) 17.2%, (b) 4.3%.

Given the close agreement of the two simulations, and given that $\nabla \cdot \boldsymbol{B} \equiv 0$ on the PS simulation, we concluded that the deviations from $\nabla \cdot \boldsymbol{B} = 0$ caused no obvious degradation of the FE solution. We were also able to make some observations on the behavior of $\nabla \cdot \boldsymbol{B}$ on the FE simulation. In particular we found that the error on $\nabla \cdot \boldsymbol{B} = 0$, which is largest along the current sheets, decreased with increasing spatial resolution. This suggests that as more resolution is applied through AMR, on the domain regions that require it, the error on $\nabla \cdot \boldsymbol{B} = 0$ can be expected to decrease. Moreover, $|\nabla \cdot \boldsymbol{B}|$ might prove useful to target domain regions that need refinement. We believe that these issues warrant further study.

Acknowledgements

The authors are thankful to R.B. Dahlburg for invaluable discussions, as well as for providing originals for the PS figures on this paper. The assistance of John Cavallo of the Scientific Visualization Studio at Goddard, to data-caputure PS spectra, is also thankfully acknowledged. This work was performed at NASA Goddard, under the HPCC ESS project.

References

[1] D. Gottlieb, M.Y. Hussaini and S.A. Orszag, in: Spectral Methods for Partial Differential Equations, eds. R.G. Voight, D. Gottlieb and M.Y. Hussaini (SIAM, Philadelphia, 1984).
[2] C. Canuto, M.Y. Hussaini, A. Quarteroni and T.A. Zang, Spectral Methods in Fluid Dynamics (Springer, Berlin, 1987).
[3] J.U. Brackbill, in: Third International School for Space Simulation: Tutorial Courses (Cepadues Editions, Toulouse, 1989) p. 183.
[4] B. Marder, J. Comput. Phys. 68 (1987) 48.
[5] J.U. Brackbill and D.C. Barnes J. Comput. Phys. 35 (1980) 426.
[6] O.C. Zienkiewicz, The Finite Element Method (McGraw-Hill, New York, 1982).
[7] C. Hirsch, Numerical Computation of Internal and External Flows (Wiley, New York, 1988).
[8] R. Löhner, Comp. Meth. Appl. Mech. Eng. 61 (1987) 323.
[9] B. Palmerio, V. Billey, A. Dervieux and J. Periaux, Self-Adaptive Mesh Refinements and Finite Element Methods for Solving the Euler Equations, Proc. ICFD Conf. on Numerical Methods for Fluid Dynamics, Reading, UK, March 1985).
[10] J.T. Oden, P. Devloo and T. Strouboulis, Comp. Meth. Appl. Mech. Eng. 59 (1986) 327.
[11] J.D. Baum and R. Löhner, Numerical Simulation of Shock-Elevated Box Interaction Using an Adaptive Finite Element Shock Capturing Scheme; *AIAA*-89-0653 (1989).
[12] R. Löhner and J.D. Baum, Numerical Simulation of Shock Interaction with Complex Geometry Three-Dimensional Structures using a New Adaptive h-Refinement Scheme on Unstructured Grids; *AIAA*-90-0700 (1990).
[13] R. Löhner, Comp. Struct. 30 (1988) 303.
[14] R. Löhner, Computer Systems in Engineering, 1 (1990) 257.
[15] R. Löhner, K. Morgan, J.Peraire and M. Vahdati, ICASE Rep. 87-4, Int. J. Num. Meth. Fluids 7 (1987) 1093.
[16] S.T. Zalesak, D.S. Spicer, R. Löhner and S. Curtis, in: Spatio-Temporal Analysis for Resolving Plasma Turbulence, ed. C.P. Escoubet (European Space Agency, Aussois, 1993) p. 315.
[17] S.A. Orszag and C.M. Tang, J. Fluid Mech. 90 (1979) 129.
[18] J. Leorat, R. Grappin, A. Pouquet and U. Frisch, in: Stellar and Planetary Magnetism, ed. A.M. Soward (Gordon and Breach, New York, 1983) p. 67.
[19] A. Pouquet, M. Meneguzzi and U. Frisch, Phys. Rev. A 33 (1986) 4266.
[20] P.-L. Sulem, A. Pouquet and M. Meneguzzi, in: Advances in Turbulence, eds. G. Comte-Bellot and J. Mathiew (Springer, 1987) p. 291.
[21] A. Pouquet, P.-L. Sulem and M. Meneguzzi, Phys. Fluids 31 (1988) 2635.
[22] R.B. Dahlburg and J.M. Picone, Phys. Fluids B, 1 (1989) 2153.
[23] D. Biskamp and H. Welter, Phys. Fluids B 1 (1989) 1964.
[24] H. Politano, A. Pouquet and P.-L. Sulam, Phys. Fluids B 1 (1989) 2330.
[25] J.M. Picone and R.B. Dahlburg, Phys. Fluids B 3 (1991) 29.
[26] J. Donea, Int. J. Numer. Methods Eng. 20 (1984) 101.
[27] R. Löhner, K. Morgan and O.C. Zienkiewicz, Int. J. Numer. Methods Eng. 4 (1984) 1043.
[28] R. Löhner, K. Morgan and O.C. Zienkiewicz, Computer Methods Appl. Mech. Eng. 51 (1985) 441.
[29] R. Löhner, K. Morgan, J. Peraire and O.C. Zienkiewicz, Finite Element Methods for High Speed Flows; *AIAA*-85-1531-CP (1985).
[30] R.D. Richtmyer and K.W. Morton, Difference Methods for Initial-Value Problems, Second Edition (Interscience Publishers, New York, 1967).
[31] M. Schmidt-Voigt, in: Interstellar Magnetic Fields, eds. R. Beck and R. Gräve, (Springer, Berlin, 1987) p. 251.
[32] M. Schmidt-Voigt, Astron. Astrophys. 210 (1989) 433.
[33] R.B. Dahlburg, private communication.